Ceramics International 51 (2025) 36573–36584

Contents lists available at ScienceDirect

Ceramics International

journal homepage: www.elsevier.com/locate/ceramint

$Cu_3Mo_2O_9$ anodes for lithium-ion batteries with extended cyclability at high rates

J. Calbet [a,b,**], C. Díaz-Guerra [c], M.L. López [a], P. Almodóvar [b], I. Álvarez-Serrano [a,*]

[a] Dpt. Química Inorgánica, Facultad de Ciencias Químicas, Universidad Complutense de Madrid, 28040, Madrid, Spain
[b] Zelestium Technologies SL, Ólvega, 42110, Soria, Spain
[c] Dpt Física de Materiales, Facultad de Ciencias Físicas, Universidad Complutense de Madrid, 28040, Madrid, Spain

ARTICLE INFO

Handling Editor: Dr P. Vincenzini

Keywords:
Copper molybdate
Mechanochemical synthesis
Lithium-ion batteries

ABSTRACT

Copper molybdate ($Cu_3Mo_2O_9$) has been synthesized through different routes, namely coprecipitation, the solvothermal method and solid-state methods using different kinds of ball-milled precursors. The effects of each synthesis route on the morphological, structural and compositional characteristics of the samples were assessed, as well as their influence on the electrochemical performance as anodes for lithium-ion batteries (LIBs). X-ray diffractometry and micro-Raman spectroscopy measurements confirmed the formation of single-phase, highly crystalline orthorhombic $Cu_3Mo_2O_9$ irrespective of the synthesis conditions, which in turn strongly influence particle size and shape, as revealed by scanning electron microscopy and transmission electron microscopy. Electrochemical tests, including cyclic voltammetry and galvanostatic charge-discharge measurements, demonstrated that $Cu_3Mo_2O_9$-based anodes show a good specific capacity and excellent cycling stability. Notably, samples obtained by mechanical milling of Cu and Mo powders followed by oxygen annealing showed a capacity of 200 mA h g^{-1} for more than 2000 cycles at a high current density of 1 A g^{-1} with coulombic efficiencies above 97 %. Such an outstanding long-term cycling performance is attributed to the high structural stability and compositional homogeneity achieved at macroscopic and local scales through the mechanical milling process, making this material a promising candidate for long-life, high-rate LIB applications.

1. Introduction

Resource depletion and the increasing energy demand are two significant global challenges that can be mitigated to a certain extent by developing advanced energy storage devices [1]. In the current energy landscape, batteries play a key role in the ways we transform, generate and utilize energy. As the world moves towards decarbonization, energy efficiency and digitalization, batteries have established themselves as fundamental elements for these processes. Historically, batteries have played a crucial role in energy portability, enabling the operation of electronic devices and vehicles in remote locations or without access to conventional energy sources. In particular, lithium-ion batteries (LIBs) - known for their high energy density, long lifespan, lack of memory effect, and environmental friendliness-have become indispensable in a broad range of applications, including portable electronic devices, electric vehicles, and large-scale energy storage systems. Over the past few decades, numerous materials, such as carbon materials, transition metal oxides, sulfides, phosphides, and lithium titanate, have been extensively studied as anode materials for LIBs. Most of these materials exhibit a specific capacity significantly higher than the theoretical one of graphite (372 mA h g^{-1}) [2]. Besides, other high-performance anode materials have also been explored for the next generation of LIBs, including alloyed materials, conversion-type transition metal composites, silicon-based composites, and carbon-based composites [3,4].

Among the different types of anodes, conversion-type anode materials (CTAMs) based on transition metals have gained prominence for LIBs [5]. These materials offer numerous attractive compositions along with a high theoretical specific capacity. Additionally, due to their lower lithium intercalation potential, CTAMs do not experience dendrite formation like graphite anodes, which may contribute to better operational safety for lithium-ion batteries. However, challenges such as poor electronic and ionic conductivity, continuous electrolyte decomposition, and relatively large volume expansion persist, limiting their practical application. Therefore, the search for more structurally stable anodes is

* Corresponding author.
** Corresponding author.
E-mail addresses: jocalbet@ucm.es (J. Calbet), ias@ucm.es (I. Álvarez-Serrano).

https://doi.org/10.1016/j.ceramint.2025.05.371
Received 18 March 2025; Received in revised form 22 May 2025; Accepted 26 May 2025
Available online 26 May 2025

of paramount importance. In this context, molybdenum-based compounds have received considerable attention as anode materials due to their rich redox chemistry involving different oxidation states (Mo^{6+} to Mo^{0}), enabling high specific capacities [6]. Specifically, molybdates exhibit good cycle stability related to their stable three-dimensional framework structure, making them promising candidates for long-term electrochemical performance [7,8]. Metal molybdates also offer many advantages, such as direct current pathways, short ion diffusion distances, low charge–discharge times, increased electrolyte-electrode contact areas, limited mechanical degradation and volume expansion accommodation [9]. Among these systems, copper molybdate ($Cu_3Mo_2O_9$), stands out due to its high theoretical capacity (916 mA h g^{-1}, more than twice the capacity of commercial graphite anodes of LIBs), superior electron conductivity and environmental friendliness.

Various strategies have been explored to enhance the electrochemical response of molybdates [7,10]. These include the preparation of nano-morphologies through alternative synthesis routes, the formation of composites with diverse carbon-based materials, and the modification of the slurry's composition, such as the use of alternative binders and/or the tuning of the active material versus additives ratio [11]. Previous studies have further advanced the electrochemical performance of copper molybdates through the design of novel morphologies and synthesis approaches. For instance, $Cu_3Mo_2O_9$ three-dimensional hierarchical flower-like structures assembled by two-dimensional nanoflakes deliver 632 mA h g^{-1} after 200 cycles at 100 mA g^{-1} with a high Coulombic efficiency [12]. Furthermore, $Cu_3Mo_2O_9$ anodes prepared by a microwave-assisted rheological phase reaction route delivered 555 mA h g^{-1} after 350 cycles at 100 mA g^{-1} [13], whereas $Cu_3Mo_2O_9$ nanoplates prepared by a pH-dependent dimensional transformation of ammonium copper molybdate attained 746 mA h g^{-1} after 120 cycles at 100 mA g^{-1} [14]. Besides, Swain et al. [15] synthesized flower-like Cu_3 $[MoO_4]_2O$ via a precursor route and demonstrated how morphological features significantly influence lithium storage behavior. Similarly, the formation of nanostructured or hierarchical morphologies in molybdates, as reported by Xiaolong et al. [16], has been shown to enhance ion diffusion and mechanical resilience during cycling, emphasizing the importance of controlled material architecture. Despite these advancements, ensuring long-term cyclability at high current densities remains a critical bottleneck for copper molybdate-based anodes. To address this issue, the present study explores various synthesis strategies for the obtaining of structurally and compositionally homogeneous $Cu_3Mo_2O_9$ with optimized performance. The influence of different preparation methods on electrochemical properties is thoroughly assessed. Notably, samples synthesized via a solid-state route using ball-milled metal powders as precursor materials demonstrated superior cycling stability and long-term performance across a range of current rates. This work provides new insights into the structure–performance relationships of copper molybdate anodes and highlights the potential of scalable synthesis methods for next-generation LIBs.

2. Materials and methods

2.1. Synthesis of materials

Various synthesis methods were employed to prepare the $Cu_3Mo_2O_9$ phases, as detailed below:

a) Ball milling of binary oxides and further annealing in air. The samples were synthesized via high-energy mechanical milling. Both binary oxides (CuO, Panreac 100 %, and MoO_3, Merck 99.5 %) were used in 3:2 stoichiometry. The milling process was carried out for 5 h at 300 rpm by using a Retsch 100 centrifugal ball mill with agate balls and vial. Subsequently, pellets of the samples (diameter ø = 1.0 cm, pressure of 5 t) underwent thermal treatments under air in a tubular furnace, first at 600 °C for 4 h, followed by 8 h at 675 °C. These samples will be termed BMO-32 hereinafter.

b) Ball milling of constituent metal powders plus subsequent annealing in oxygen atmosphere (BMM-32 samples). Cu (Panreac, 99.5 %) and Mo (Merck, 99.7 %) powders in 3:2 stoichiometry were mixed and milled by using the same system and conditions specified for the previous samples. After this stage, the synthesis procedure was similar to the one described above, but in this case thermal treatments were carried out under a continuous oxygen flow.

c) Solvothermal synthesis (ST-32 samples). The solvothermal synthesis was conducted by dissolving 0.682 g of $Cu(NO_3)_2{\cdot}4H_2O$ (Merck, 99.5 %) and 0.387 g of $Na_2MoO_4{\cdot}2H_2O$ (Sigma Aldrich, 98 %) in a 50:50 mixture of deionized water and ethanol (ChemLab, 98 %). The mixture was transferred into a sealed autoclave and heated at 180 °C for 15 h. After natural cooling, the product was filtered, dried at 50 °C, and finally calcined at 500 °C for 6 h in an air atmosphere.

d) Coprecipitation synthesis (Copre-32 samples). In this case, 5 mmol of copper acetate ($CuAc_2$, Sigma Aldrich, 98 %) were dissolved in 20 mL of deionized water, and 10 mL of a 5 mmol sodium molybdate solution were added dropwise under continuous stirring. Then, 5 mL of ethylene glycol (Scharlau, 100 %) were added. After 20 min of stirring, the precipitate was filtered, washed with deionized water and acetone, and dried at 110 °C for 16 h. Finally, the product was calcined at 500 °C for 6 h in air.

Table 1 summarizes the synthesis methodologies and thermal treatments applied for the preparation of the investigated materials, together with sample naming. Each of the four growth methods involves specific synthesis conditions designed to optimize the structural and chemical properties of the samples.

2.2. Preparation of the electrodes

For the electrochemical measurements, the anode materials were prepared by mixing 55 wt% of the active material (0.5–3 mg) with 25 wt % of carbon super P (Imerys Graphite & Carbon, Bironico, Switzerland) and 20 wt% of sodium alginate (Sigma Aldrich) with a small amount of distilled water and then coated directly on the copper foil support of a Swagelok cell and dried for 2 h. This proportion was carefully selected after testing other proportions of active material, carbon and binder. Pristine carbon additive was also electrochemically tested separately, confirming that its contribution to the total capacity could be neglected, within the experimental error. Sodium alginate is a cost-effective, environmentally friendly binder. Electrodes made of α-MoO_3 composites and Na alginate were reported to exhibit much better electrochemical performance than those composed of conventional polyvinylidene fluoride (PVDF) [11,17]. The suitability of Na alginates as a binder has been demonstrated in the case of Al-ion batteries as well [18,19]. Such improved electrochemical performance was attributed to its unique structural features, which facilitate the formation of a homogeneous 3D networking between the conductive agent and active material particles. This results in a tightened electrode architecture which contributes to stabilizing storage capability [17–19]. Besides, the use of sodium alginate has been shown to enhance the homogeneity of

Table 1
Sample naming and synthesis conditions of the investigated materials.

Name	Preparation	Thermal treatment
BMM-32	Ball-milling from metals	600 °C/4 h + 675 °C/8 h under O_2
BMO-32	Ball-milling from MoO_3 and CuO oxides	650 °C/24 h + 675 °C/8 h in air
ST-32	Solvothermal synthesis from Na_2MoO_4 and Cu $(NO_3)_2$ in 50 % ethanol/50 % H_2O)	180 °C/15 h + 500 °C/6 h in air
Copre-32	Coprecipitation from $CuAc_2$ and Na_2MoO_4 in ethyleneglycol	110 °C/16 h + 500 °C/6 h in air

the slurry, also avoiding the use of nonaqueous solvents in the composite preparation process. The electrodes were prepared with slurry loadings of approximately 2 mg (~1.7 mg cm^{-2}). All the components of the Swagelok cell were assembled inside an argon-filled dry box in sequence, starting with the as-prepared coated electrode, followed by a Whatman borosilicate glass fiber sheet (grade GF/D) soaked with drops of 1 M $LiPF_6$ in ethylene carbonate (EC) and dimethyl carbonate (DMC) (1:1 by weight) as the electrolyte, and finally, a lithium metal counter electrode.

2.3. Characterization methods

Long-range and short-range structural characterization of the samples was respectively carried out by X-ray diffractometry (XRD) and micro-Raman spectroscopy. XRD measurements were performed by using a PHILIPS X'pert-MPD diffractometer with Cu-Kα radiation ($\lambda K\alpha_1 = 1.5418$ Å). The XRD patterns were acquired with 0.05° scanning steps and a 1-s dwell time. Data analysis was carried out by using the PC-APD software and compared with reference patterns from the Inorganic Crystal Structure Database (ICSD). Raman measurements were performed with a Horiba Jobin-Yvon LabRam HR 800 system on an Olympus BX 41 confocal microscope at room temperature. The samples were excited by a HeNe laser at 633 nm, carefully adjusting power density in order to maximize signal to noise ratio while avoiding laser-induced structural and compositional changes.

The morphology and composition of the samples were analyzed by scanning electron microscopy (SEM) with a Hitachi TM3000 microscope operating at 15 kV and equipped with a backscattered electron (BSE) detector. Energy dispersive X-ray microanalysis (EDS) measurements were performed by using a Bruker QUANTAX 70 EDS detector attached to the mentioned SEM. Data was processed with the ESPRIT QUANTAX 70 software. High-resolution transmission electron microscopy (HRTEM) and electron diffraction (ED) patterns were obtained using a JEOL JEM 3000 operating at an accelerating voltage of 300 kV. Samples were prepared by crushing the powders under n-butanol and dispersing them over copper grids covered with a porous carbon film. Semi-quantitative chemical analyses and compositional mappings were carried out using EDS in STEM mode.

Electrochemical studies were conducted using cyclic voltammetry (CV) and charge-discharge cycles, utilizing a Swagelok-type assembly with a copper current collector. The tests were carried out by using either an Arbin® BT-2143 or a Biologic® BCS-815 battery tester. Specific capacity and coulombic efficiency were calculated at different current densities. Electrochemical Impedance Spectroscopy (EIS) data were acquired with the Biologic BCS-815 battery tester by applying an AC voltage of 5 mV over a frequency range of 0.01–100 kHz. The acquired data were subsequently analyzed using the BT-Lab software.

3. Results and discussion

As explained above, $Cu_3Mo_2O_9$ samples were obtained following different synthesis routes. Although the structure and composition of these samples were found to match those of the title compound (*vide infra*), only BMM-32 material exhibits a remarkable electrochemical behavior. Fig. 1 gathers the corresponding XRD profiles and representative micro-Raman spectra of all the samples investigated. XRD patterns.

(Fig. 1a) shows rather narrow and well-defined diffraction maxima, which is indicative of the good crystallinity of the samples and their homogeneous crystal structure. All the Bragg peaks could be readily indexed to the orthorhombic structure of $Cu_3Mo_2O_9$ with *Pnma* space group (PDF 70–2493). The structure (Fig. 1b) can be described based on the assembly of $[MoO_4]$ and $[CuO_6]/[CuO_5]$ polyhedra, resulting in a well-organized framework. In order to get further insight into the structure of the samples at local level and to detect the possible existence of minority phases and/or phases with low crystallinity, micro-Raman spectroscopy measurements were also carried out. Fig. 1c shows representative spectra of all the prepared materials. Main peaks appear centered at about 99, 140, 264, 326, 362, 498, 810, 837, 861, 892, 933 and 957 cm^{-1}. The strongest peaks in the (800–1000) cm^{-1} range can be attributed to the stretching vibrations of the $[MoO_4]$ tetrahedra. The number of maxima in this spectral range and the corresponding peak positions allow to clearly distinguish $Cu_3Mo_2O_9$ from other Cu molybdates, such as $CuMoO_4$, and Mo oxides. In the (200–500) cm^{-1} range, less intense peaks, associated to deformation modes involving $[CuO_6]$ and $[CuO_5]$ octahedra, can also be observed. The number and position of the observed vibrational modes are consistent with the *Pnma* crystal structure of $Cu_3Mo_2O_9$ [20,21], while the absence of additional unassigned peaks and the small width of the observed Raman bands are indicative of single-phase materials with a low defect concentration, in agreement with XRD measurements. It should be mentioned that this is the case for all $Cu_3Mo_2O_9$ samples grown in the present work, irrespective of the synthesis route (hydrothermal, co-precipitation, solid state) followed, as revealed by XRD and Raman results shown in Fig. 1. Nevertheless, SEM images reveal that both the synthesis route and the starting reagents or precursor materials strongly influence the final morphology of the samples (Figs. 2 and 3). Well-sintered grains with sizes in the (2−10) μm range are shown in SEM images of the BMM-32 material (Fig. 2a). Besides, Cu, Mo and O, EDS spectra (Fig. 2b) only reveal minute amounts (note the logarithmic scale) of Si and Al, which might be incorporated from the alumina boat used to anneal the samples. Semi-quantitative analyses reveal a Cu:Mo ratio of 1.5, which is nominally equal to the expected stoichiometric value, while corresponding EDS mappings (Fig. 2c and d) show a homogeneous Cu and Mo spatial distribution. Similar EDS results were obtained in the different samples.

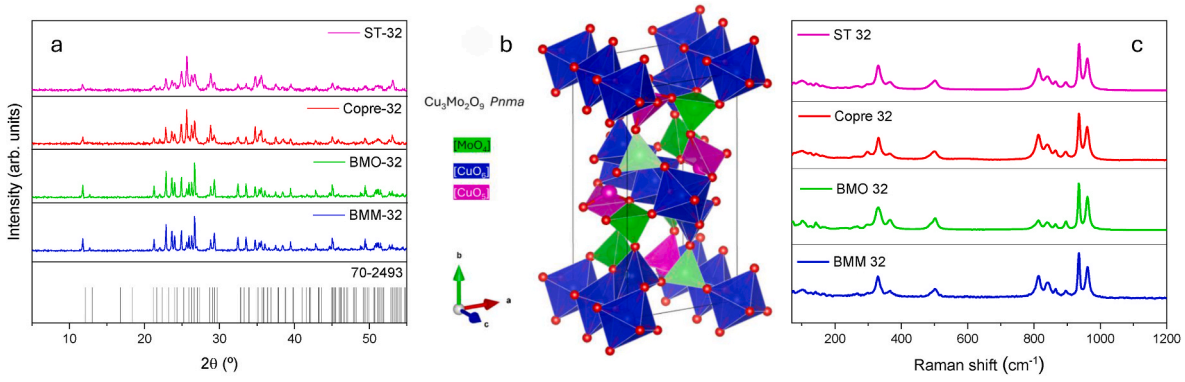

Fig. 1. a) XRD profiles of BMM-32, BMO-32, Copre-32 and ST-32 samples and reference $Cu_3Mo_2O_9$ PDF file (70–2493), b) crystal structure of $Cu_3Mo_2O_9$, space group *Pnma,* and c) representative Raman spectra of the grown samples.

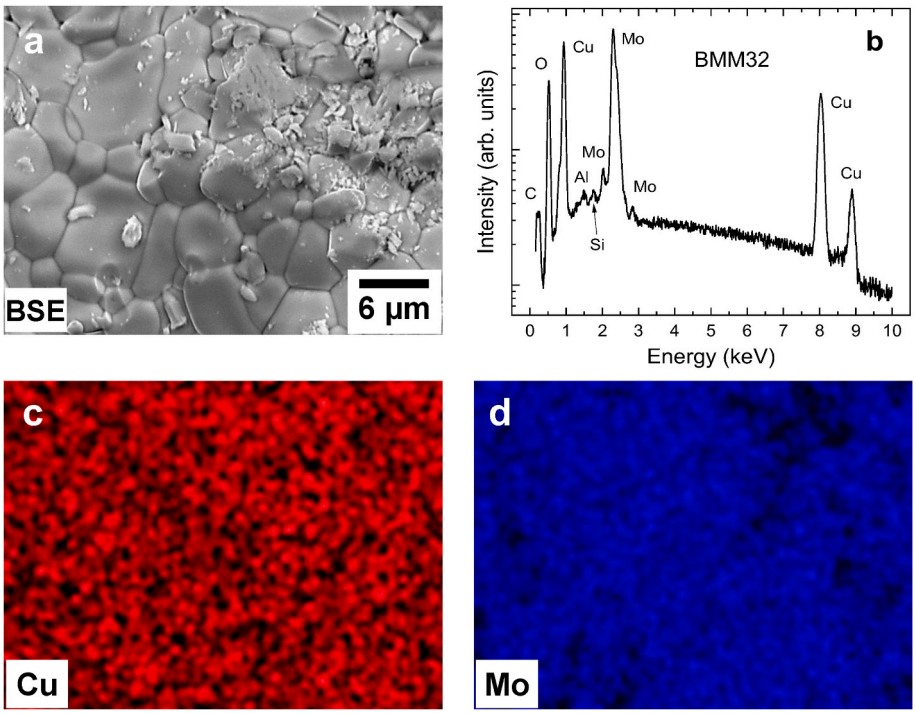

Fig. 2. a) Representative BSE image of a BMM-32 sample; b) EDS spectrum represented in log scale to clearly visualize elements present in very low concentrations, c) d) corresponding Cu and Mo compositional maps.

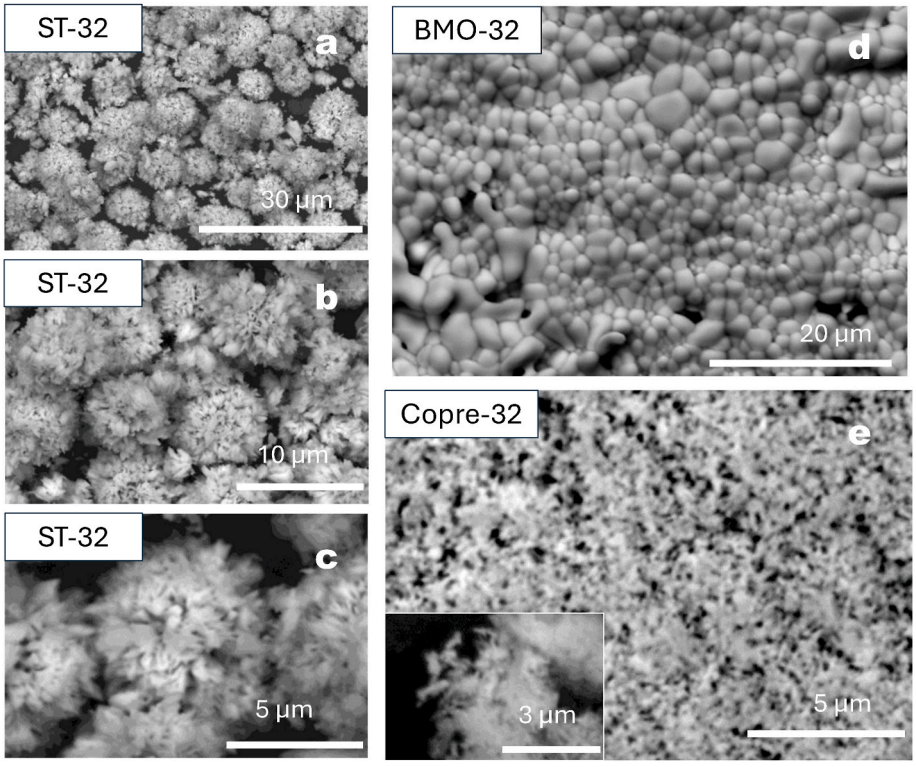

Fig. 3. Representative BSE images of samples ST-32 (a–c), BMO-32 (d) and Copre-32 (e).

Fig. 3 shows representative SEM images of the ST-32, Copre-32 and BMO samples. The BMO-32 sample exhibits a granular morphology similar to that of BMM-32, although with slightly larger grains and a less compact structure. However, ST-32 sample displays a microstructure composed of dandelion-like formations, assembled from aggregated needle-like submicron particles. Meanwhile, Copre-32 features similar needle-like structures, but more uniformly dispersed across a highly porous and less cohesive matrix. These morphological differences are relevant for the understanding of the electrochemical behavior, since surface porosity, grain connectivity, and compactness can greatly

influence lithium-ion transport, structural stability, and long-term cycling performance.

As stated before, SEM images show a homogeneous distribution of the constituent elements. However, it is important to note that the inherent resolution of the SEM-EDS analysis can make it difficult to identify minor phases or structural defects at the sub-micrometric scale. For this reason, additional structural and compositional analysis was carried out by TEM, which allows observation at the nanometer scale of morphological features, particle size, phase distribution and structural defects, which are key to unveiling the relationship between the microstructure of the material and its electrochemical performance. Fig. 4 and Fig. S1 show selected TEM results for the BMM-32 material. The images, along with the corresponding electron diffraction (ED) patterns, are consistent with the orthorhombic symmetry and cell parameters previously described for $Cu_3Mo_2O_9$. A representative high-resolution TEM (HRTEM) image and its associated ED pattern are shown in Fig. 4a. Measured distances of 0.73 nm and 0.39 nm respectively correspond to the (020) and (200) interplanar spacings, which are characteristic of the orthorhombic $Cu_3Mo_2O_9$ structure. Additionally, it is worth highlighting the sample's high crystallinity, which is free from extended defects. On the other hand, EDS STEM mappings (Fig. 4b) reveal a high compositional homogeneity at the nanometer scale, indicating a uniform distribution of the constituent elements along the structure. These results confirm the effectiveness of the BMM-32 synthesis process in producing highly crystalline and compositionally uniform $Cu_3Mo_2O_9$ material.

To evaluate the electrochemical behavior of the materials obtained through different synthesis methods, an initial set of four CV measurements at a sweep rate of 0.1 mV s^{-1} was performed. Fig. 5a shows four consecutive cycles for the BMM-32 anode in the potential range of 0.01–3.00 V.

Two cathodic peaks appear in the first cycle at about 2.5 and 1.5 V, but they are no longer observed in subsequent cycles. As previously suggested by Liu et al. [12,13], these peaks can be related to the formation of the Solid Electrolyte Interface (SEI) and to irreversible processes that give rise to the formation of a Li-Cu-O phase and an electrochemically active phase, $Li_xCu_3Mo_2O_9$ or Li_xCuMoO_4. In subsequent cycles, a cathodic peak at about 0.5–0.6 V and an anodic peak at about 1.5–1.7 V are observed, which correspond to different redox processes associated with the presence of Mo and Cu. A conversion mechanism according to the following sequence of reactions is hence proposed to be responsible for the observed behavior, which is similar to those proposed for other mixed metal oxides in LIBs [12,14]:

$$Cu_3Mo_2O_9 + xLi^+ + xe^- \rightarrow Li_xCu_3Mo_2O_9$$

$$Li_xCu_3Mo_2O_9 + (18-x)Li^+ + (18-x)e^- \rightarrow 3Cu + 2Mo + 9Li_2O$$

$$Mo + 3Li_2O \leftrightarrow MoO_2 + 6Li^+ + 6e^-$$

$$MoO_2 + Li_2O \leftrightarrow MoO_3 + 2Li^+ + 2e^-$$

$$Cu + Li_2O \leftrightarrow CuO + 2Li^+ + 2e^-$$

Therefore, once the first cycle is finished, the initial conversion reaction gives rise to the stabilization of a Cu-Mo-O phase in which lithium ions can be intercalated and deintercalated. This process can take place mostly at the surface or also within the bulk anode material, potentially leading to diffusive/capacitive characteristics. The redox peaks observed in the curves shown in Fig. 5a are not very sharp or well-defined, pointing towards pseudocapacitive behavior dominated by surface storage mechanisms and diffusive redox processes. To make a preliminary kinetic assessment, additional CV measurements were carried out at different sweep rates (Fig. 5b). The CV profiles show the same features for all the scan rates tested, suggesting a good electrochemical stability of the cell [22]. The relationship between the current and the sweeping rate can be expressed in terms of the following law [23,24]:

$$i = a \cdot \nu^b$$

where i is the peak current, ν refers to the sweep voltage rate and a and b are adjustable parameters. This equation can be rewritten as follows:

$$\log(i) = \log(a) + b \cdot \log(\nu)$$

In this way, by linear fitting of $\log(i)$ vs. $\log(\nu)$, the values of a and b can be obtained from the corresponding ordinate and slope. The parameter a depends on the nature of the electrochemical system, while b is a constant which can be related to the predominant mechanism of

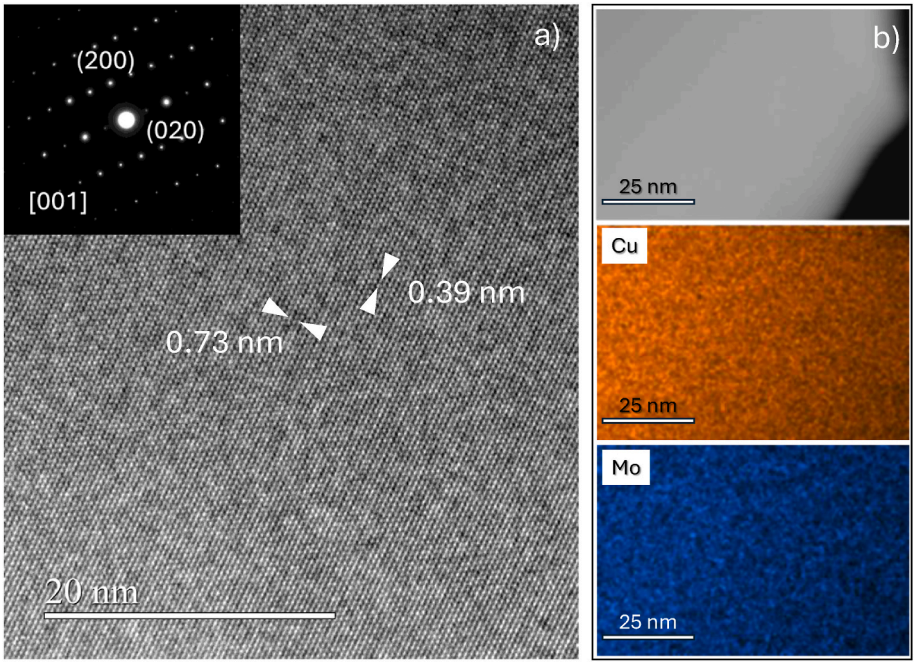

Fig. 4. a) HRTEM image of BMM-32 sample. The inset shows the corresponding ED pattern. b) STEM image of a particle of the same material and the related compositional Cu and Mo EDS mappings.

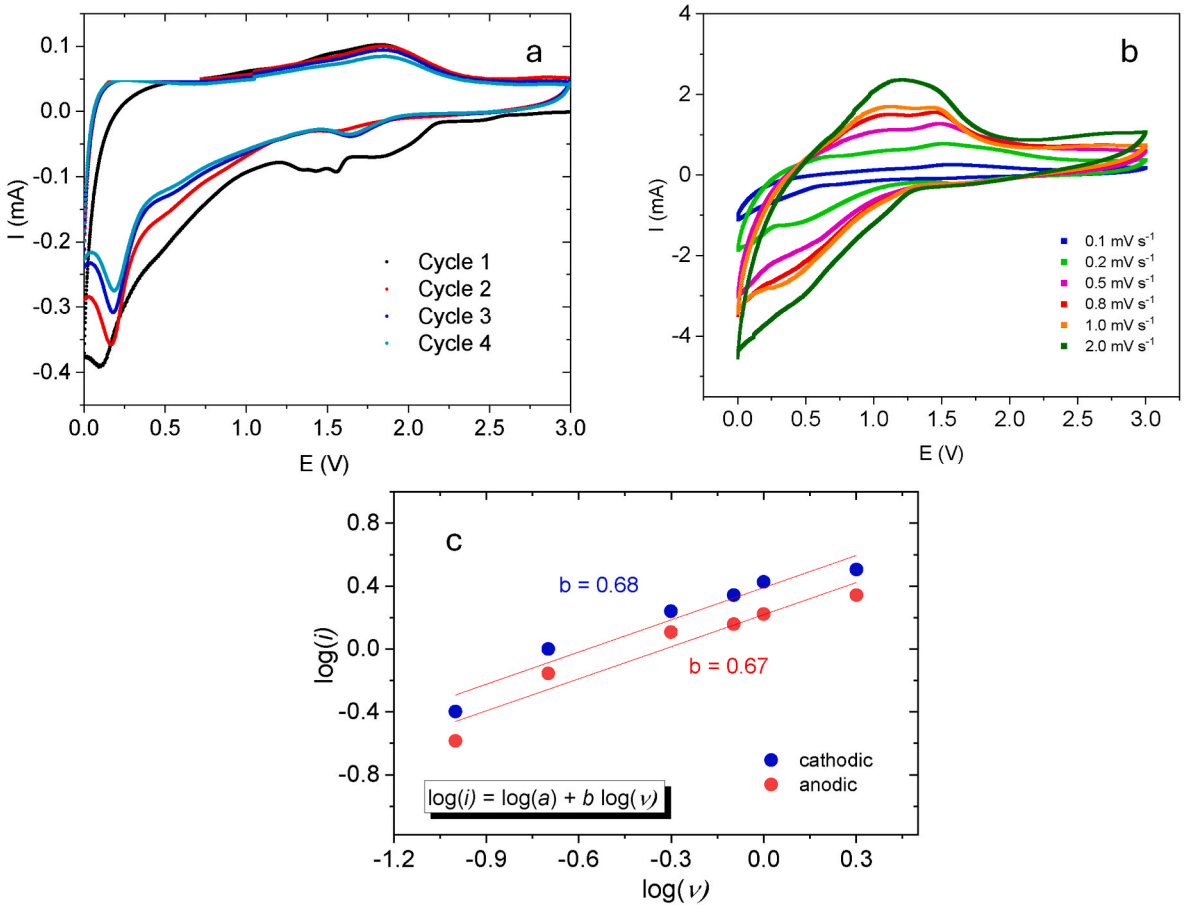

Fig. 5. a) Consecutive CVs of sample BMM-32 32 at 0.1 mV s^{-1}, b) CV curves at different sweep rates, c) linear fits and *b* parameter values for BMM-32.

the process. Thus, *b* is equal to 1 for a capacitance-controlled process, *i.e.* a capacitor, whereas it is equal to 0.5 for a process dominated by a diffusive mechanism, *i.e.,* a process in which ions diffuse into the material, such as an electrode consisting of an insertion material. Therefore, the value of *b* indicates the predominant mechanism of charge storage. Fig. 5c shows the corresponding fittings for the main anodic and cathodic processes in BMM-32 electrode. The *b* values obtained were 0.68 and 0.67, respectively. These values agree with those previously reported for related systems [13], suggesting that the current response of the electrode is mainly due to the contribution of the capacitive behavior. Moreover, the current response under a given voltage can be attributed to two components: capacitive and diffusion-controlled, as described by the following equation [25]:

$$i = k_1\nu + k_2\nu^{0.5}$$

here, k_1 and k_2 are adjustable parameters that can be determined from

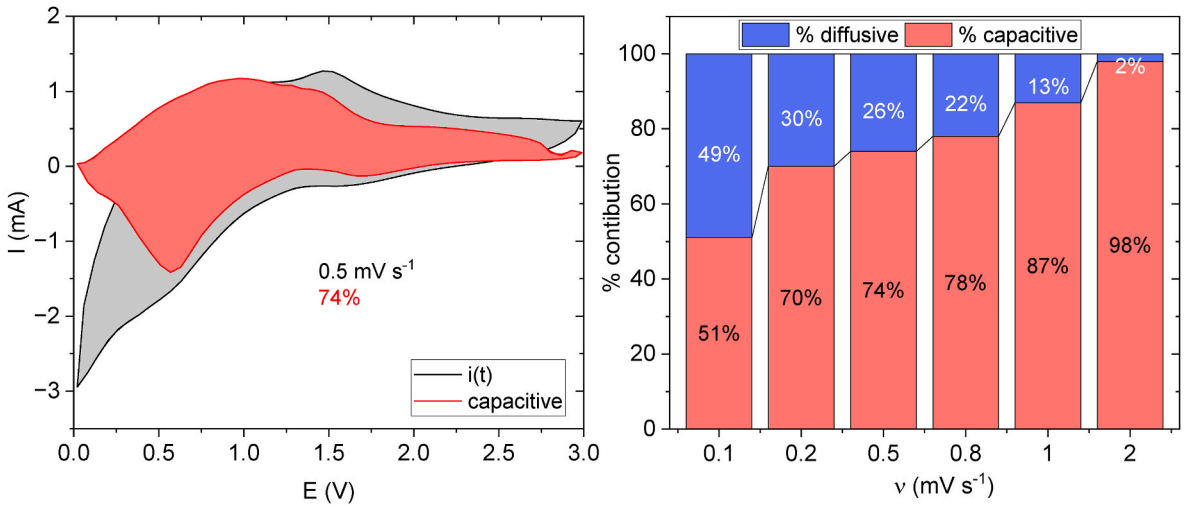

Fig. 6. a) BMM-32 electrode CV curve measured at a scan rate of 0.5 mV s^{-1}, showing capacitive-controlled contribution. b) Capacitive and diffusion-controlled contribution fractions versus scan rate.

the slope and y-intercept of the fitted $i\,v^{-0.5}$ vs. $v^{0.5}$ plots, respectively. The term $k_2\nu$ represents the capacitive contribution whereas $k_1\,v^{0.5}$ corresponds to the capacity component governed by diffusion-controlled processes. Using this method, the capacitive contribution to the capacity of the BMM-32 electrode at various scan rates was calculated. The corresponding results are shown in Fig. 6 and Fig. S2. The BMM-32 anode exhibits predominantly capacitive behavior, consistent with the shape of the CV curves and the obtained *b* values, as explained above.

Aiming to analyze the electrochemical performance of the different anode materials prepared, galvanostatic charge-discharge experiments at different current rates were carried out. In order to compare the electrochemical response of the synthesized materials, the following sequence was applied in all cases: 10 cycles at 0.1 A g^{-1} followed by 10 cycles at 0.2 A g^{-1}, then 10 cycles at 0.5 A g^{-1} and, finally, 100 cycles at 1 A g^{-1}. Fig. 7 shows the corresponding curves for the mentioned current densities of 0.1, 0.2, 0.5, and 1 A g^{-1}, while Table 2 summarizes the obtained capacity values for selected cycle numbers corresponding to the different anode materials. As expected, the specific capacitance values gradually decrease as the current density increases. At low current rates, where electrochemical processes are controlled and ion transport is more efficient, the highest specific capacity of the material is reached, showing an adequate performance under optimal ionic diffusion conditions. However, when the current rate progressively increases, the specific capacity decreases, since the insertion and extraction of ions is not efficiently completed for shorter times. Regarding capacity retention, calculated as the ratio between capacity values at a selected cycle number and at the first cycle (Table 2), the obtained values at moderate and low current rates are comparable for all samples. However, at higher rates (such as 1 A g^{-1}), Copre-32 anode demonstrates better capacity retention, despite exhibiting lower absolute capacity values, as compared to the BMM-32 anode. Considering both capacity and retention characteristics, the BMM-32 anode exhibits the best overall electrochemical performance among the synthesized $Cu_3Mo_2O_9$ materials.

Several relevant figures for previously reported Cu-Mo-O and Mo-based anodes are summarized in Table 3 and compared with the electrodes which in our case show the best response at both moderate (0.1 A g^{-1}) and high (1 A g^{-1}) current rates, namely BMM-32 and Copre-32. Results obtained in the present work can be considered as highly promising, especially at high rates, as compared with those previously obtained for similar Cu-Mo mixed oxides [7].

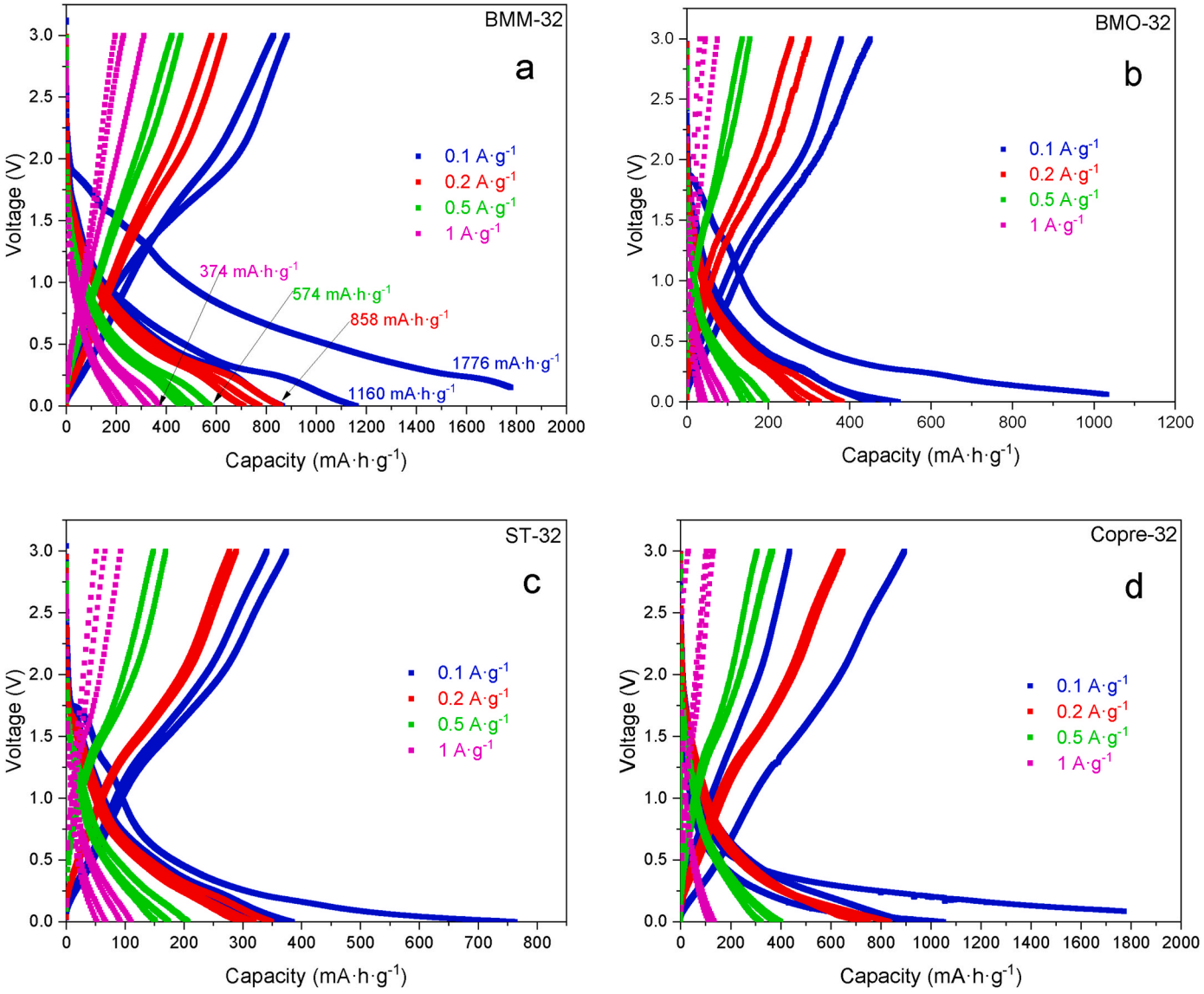

Fig. 7. First, second and last (10th or 100th, depending on rate) charge and discharge cycles at different current densities for a) BMM-32, b) BMO-32, c) ST-32 and d) Copre-32 samples.

Table 2
Discharge capacity values (Q_d) at selected cycles numbers [N], and capacity retention values {Q}, for the prepared $Cu_3Mo_2O_9$ anodes.

Sample	Q_d[a] 0.1 A g^{-1} (mA·h·g^{-1}) [Cycle] {% Q_{10}}[b]	Q_d 0.2 A g^{-1} (mA·h·g^{-1}) [Cycle] {% Q_{10}}	Q_d 0.5 A g^{-1} (mA·h·g^{-1}) [Cycle] {% Q_{10}}	Q_d 1 A g^{-1} (mA·h·g^{-1}) [Cycle] {% Q_{100}}[c]
BMM-32	1776 [1] - 1159 [2] 864 [10] {49}	858 [1] - 775 [2] 710 [10] {83}	574 [1] - 502 [2] 461 [10] {80}	374 [1] - 327 [2] 206 [100] {55}
BMO-32	1031 [1] - 519 [2] 456 [10] {44}	382 [1] - 325 [2] 285 [10] {75}	197 [1] - 162 [2] 140 [10] {71}	97 [1] - 77 [2] 33 [100] {34}
ST	762 [1] - 361 [2] 383 [5] {50}	348 [1] - 319 [2] 299 [10] {86}	207 [1] - 173 [2] 151 [10] {73}	110 [1] - 91 [2] 52 [100] {47}
Copre-32	1771 [1] - 1049 [2] 912 [10] {51}	832 [1] - 750 [2] 735 [10] {88}	399 [1] - 377 [2] 321 [10] {80}	134 [1] - 133 [2] 105 [73] {78}

[a] Maximum capacity obtained during the discharge process.
[b] Capacity retention after 10 cycles.
[c] Capacity retention after 100 cycles.

Indeed, at a current rate of 0.1 A g^{-1}, both BMM-32 and Copre-32 anodes deliver specific capacity values close to 1770 and 900 mA h g^{-1} after the first and the tenth cycle, respectively. Besides, at a high current rate of 1 A g^{-1}, BMM-32 delivers a capacity of ca. 200 mA h g^{-1} even after 100 cycles, whereas the Copre-32 anode shows a lower first capacity value of about 130 mA h g^{-1}. Considering the cycling behavior of the different anodes, *i. e* the capacity fading through cycling at each current rate and the coulombic efficiency obtained (which remained close to 100 % throughout cycling), BMM-32 anode was selected for exploring long-term performance, particularly at high current rates. Fig. 8 shows the obtained charge and discharge capacities together with the coulombic efficiency values through more than 2300 cycles according to the following sequence: 10 cycles at 0.1 A g^{-1}, followed by 10 cycles at 0.2 A g^{-1}, then 10 cycles at 0.5 A g^{-1}, followed by 2070 cycles at 1 A g^{-1}, then 100 cycles at 2 A g^{-1}, 100 cycles at 1 A g^{-1} and 15 cycles at 0.1 A g^{-1} to finish the experiment. As can be appreciated, after 2000 cycles at different current rates, the recovery of capacity values when returning to 0.1 A g^{-1} is excellent, *i.e.* 650 mA h g^{-1}, with coulombic efficiencies ranging between 97 % and 99 % throughout the whole cycling sequence.

Results shown in Fig. 8 evidence the high cyclability of the BMM-32 samples, with stable capacity values of about 200 mA h g^{-1} for more than 2000 charge/discharge cycles. We are not aware of previous works reporting such an extended cyclability at any current rate in any Cu-Mo mixed metal oxide. Actually, only Zhang. et al. [12] tested $Cu_3Mo_2O_9$ samples up to 350 cycles and at a maximum, limited current rate of 0.2 A g^{-1}, *i. e*, a seven times lower number of cycles and an order of magnitude lower current density than those used in the present work. In fact, this is a remarkable performance which corresponds to what is frequently termed "ultra-long cycling" in the literature, referring to electrodes that retain stable capacities over thousands of cycles [27,28]. Outstanding electrochemical performances of that kind have previously been observed mainly for niobium-based materials, such as Nb_2O_5, where ultra-long cycling at high current densities has been attributed to pseudocapacitive behavior and enhanced ionic/electronic transport [29,30]. However, niobium is classified as a critical raw material, with limited availability and high cost. Our results suggest that comparable cycling performance can be achieved without relying on critical elements, using more sustainable and abundant metals like Cu and Mo. In particular, the BMM-32 sample here reported was prepared using a ball-milled stoichiometric mixture of Cu and Mo metal powders, which was subsequently annealed in oxygen flow. Mechanochemical synthesis is a well-stablished approach to achieve safer, cleaner and more efficient transformations, avoiding the necessity of reactants or bulk dissolutions. Due to its efficiency and unique reactivity, mechanochemical processing of bulk solids has developed into a scalable, powerful tool for the synthesis and transformation of various types of materials, including metals. In particular, ball milling frequently offers an enclosed solvent-free reaction environment with well-defined parameters for optimizing reactivity (balls to sample weight ratio, milling time, rotation speed, etc.) [31]. One of the novelties here reported is the application of ball milling to the preparation of the precursor material used to obtain the mixed oxide. Such precursor is usually a mixture of un-milled binary oxides when the solid-state route is followed, while in our case metal powders are mixed and milled to obtain the starting material. Although solid-state synthesis of mixed Cu-Mo oxides has previously been reported in the literature, the synthesis strategy followed so far was based on the annealing at high temperature of binary oxide powders, either previously ball-milled or not [6,32]. The material here prepared follows a different approach: for almost immiscible alloy systems with high heats of mixing, such as Cu-Mo, the solubilities are extremely low. Actually, it has been observed in Cu-10 at.% Mo alloys, that Mo atoms do not show any tendency of diffusion along Cu dislocation lines and, in consequence, Cu-Mo alloys show no sign of a formation of a solid solution, even after long milling times [33]. However, previous works on powder ball milling in alloys indicate that this treatment increases the distortion energy, influencing the sintering densification. Precisely, in Mo-W-Cu alloys a moderate ball milling time (~10 h) is able to

Table 3
Synthesis method, morphology and electrochemical performance as LIBs electrodes of Cu/Mo-based oxides reported in the literature and in the present work.

Electrode	Preparation Method	Morphology	Rate (A·g^{-1})[a]	Q (mA·h·g^{-1}) [Cycle number]	Ref.
$Cu_3Mo_2O_9$	HT + 700 °C	3D hierarchical flowers	0.1	630 [10]	[12]
			1	519 [35]	
$Cu_3Mo_2O_9$	Microwave + 500 °C	Granular (100–400) nm	0.2	555 [350]	[13]
			1	200 [10]	
$Cu_3Mo_2O_9$	HT	Nanoplates	0.1	720 [50]	[14]
			0.5	455 [10]	
$Cu_3Mo_2O_9$	Calcination + PANI[b] Coating	Cuboids	0.1	800 [200]	[21]
			1.6	290 [10]	
$CaMoO_4$	Hydrothermal + Ni foam	Nanorods, sheet-like microstructures	0.5	450 [10]	[16]
MoO_2/CNFs	Electrospinning with carbon nanofibers + annealing	Nanofibers	0.1	636 [100]	[26]
BMM-32	Ball milling of metals + annealing in oxygen @650 °C	Rounded grains (2−10) μm	0.1	854 [10]	This work
			0.5	461 [10]	
			1	206 [100]	
Copre-32	Coprecipitation + annealing @500 °C	Nano pseudospheres	0.1	912 [10]	This work
			1	100 [70]	

[a] Current density.
[b] PANI: polyaniline polymer.

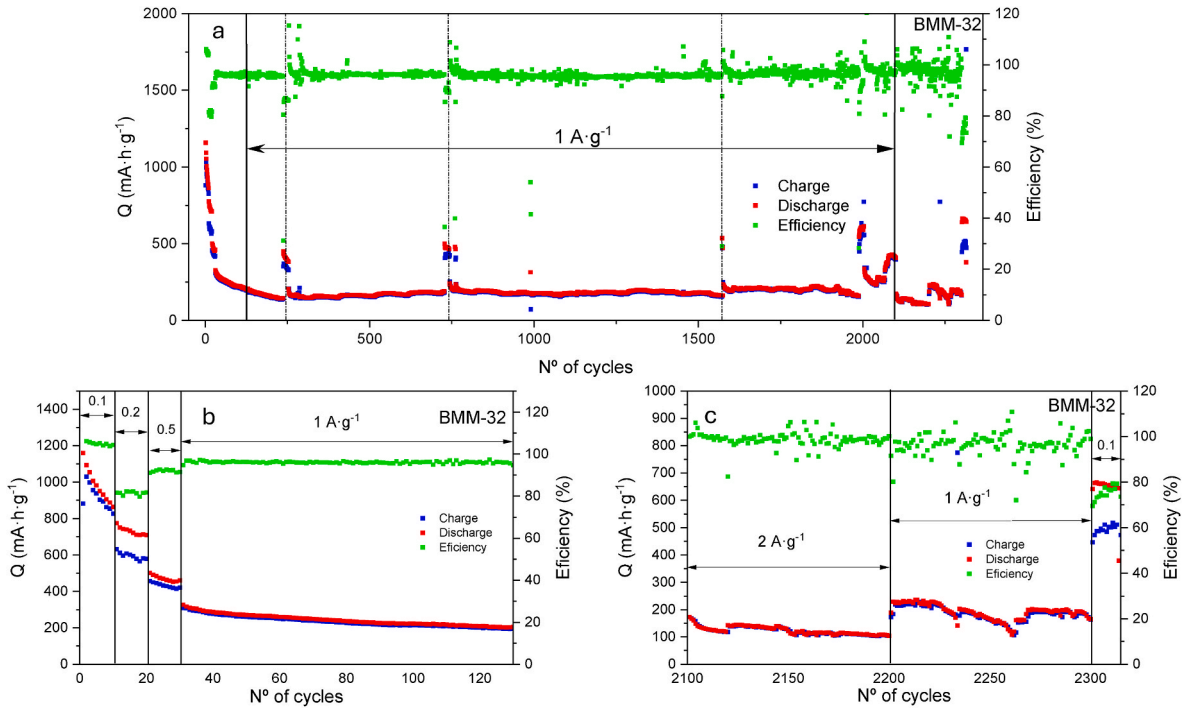

Fig. 8. a) Long-term discharge-charge cycling at different current rates, b) and c) zoomed view in a selected range of cycle numbers. Continuous vertical lines indicate the limits of the applied current rates. Dashed vertical lines indicate 1 h of holding in cycling. Current densities are expressed in all cases in A g^{-1}.

effectively refine the particle size and improve the uniform distribution of the alloy powder elements, largely contributing to the obtaining of a dense and homogeneous microstructure [34]. Moreover, mechanical activation caused by ball-milling is attributed to macro- and micro-scale changes, such as particle size, specific surface area, crystallographic structure, etc. The active mechanical energy is partially transferred to the particles, either by the impact of solid particles or by induction of tensile and compressive stresses in powder mass. The mechanical energy might lead to the occurrence of structural defects such as changes of the surface, lattice distortion and conversion of long range order to short range order. Therefore, the free energy or chemical potential gained can change during the mechanical activation. In this way, the solid systems reach an activated state, which could accelerate the reaction in subsequent processes, especially oxidation and recrystallization behaviors [35]. For instance, previous reports have demonstrated that ball-milling treatment enhances the oxidation rate of Ag–Zn alloy powders due to the increase of dislocation density and the decrease of the diffusion distance of oxygen during internal oxidation [36]. As can be deduced from the XRD, Raman spectroscopy and SEM results, this sample has a high compositional and structural homogeneity at macroscopic and local scales, probably due to the intimate grinding process before oxidation. The electrochemical response could therefore be related to the high homogeneity of the material, allowing the preparation of a composite with high structural stability.

In order to get insight into kinetics of the electrochemical processes, EIS measurements were performed in all the prepared anodes. As reported in the literature [11], lithium diffusion coefficients (D) can be estimated from EIS data by using the following equation:

$$D = \frac{R^2 T^2}{2A^2 n^4 F^4 C^2 \sigma^2}$$

where R is the gas constant (8.314 J K^{-1} mol^{-1}), T is the absolute temperature (293 K), A is the surface area of the electrode (1.32 cm^2), n corresponds to the number of electrons transferred in the redox reaction (18), F is the Faraday constant (96.486 C mol^{-1}), C is the lithium ion concentration in the electrode and σ is the Warburg factor, which is related to Z' (real part of impedance). σ can be obtained from the slope of the linear fit of Z′ at low frequencies plotted as a function of $\omega^{-1/2}$:

$$Z' = R_1 + R_2 + \sigma\, \omega^{-0.5}$$

where R1 and R2 refer to high and medium-frequency components, respectively, that will be addressed later. Fig. 9a shows the corresponding Nyquist plots for the prepared composite electrodes after five discharge-charge cycles, while the corresponding fittings are shown in Fig. 9b. Based on the obtained σ values, the calculated Li-ion diffusion coefficients are 4.5×10^{-12}, 4.4×10^{-14}, 2.3×10^{-14} and 6.2×10^{-15} cm^2 s^{-1} for the BMM-32, Copre-32, BMO-32 and ST-32 electrodes, respectively. The obtained values are in good agreement with those previously reported for similar materials [11,37] and are also coherent with the observed electrochemical response (Fig. 7). Accordingly, the BMM-32 electrode, which exhibits the best electrochemical performance, also shows the highest Li-ion diffusion coefficient. This indicates that the structural and compositional characteristics of this sample favor enhanced lithium transport, thereby contributing to its superior electrochemical behavior. Nevertheless, we would like to remark that this approach should be applied with caution in the case of conversion and alloying materials, as these systems usually involve multiple phases with varying molar volumes. Consequently, the obtained coefficients should be regarded as rough estimations.

To investigate the phase evolution throughout the electrochemical process, a preliminary *ex-situ* XRD analysis was performed on the BMM-32 electrode composite before and after cycling. Fig. S3 shows the corresponding XRD patterns. As previously noted for this kind of materials [12], the conversion-type reactions involved in the electrochemical response of the anodes typically result in poorly crystalline phases that are challenging to detect by XRD. Indeed, the post-cycled electrode exhibited only weak diffraction signals. Nevertheless, Bragg peaks observed around 32° and 39° may correspond to Li_2O (PDF 01-074-0115), thereby supporting a conversion mechanism for the process.

To identify possible structural changes and the appearance of different phases after cycling more clearly, an *ex-situ* micro-Raman study

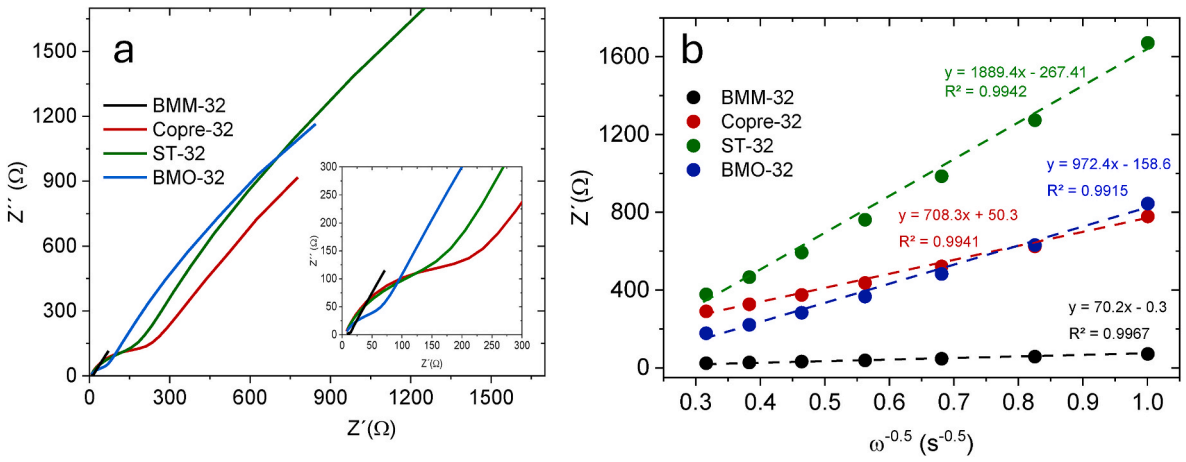

Fig. 9. a) Impedance Nyquist plots for the investigated $Cu_3Mo_2O_9$ electrode materials (after 5 cycles at 0.1 A g^{-1} rate). The inset shows a zoomed view of the high-frequency region; b) Linear fittings of the real part of the complex impedance (Z ′) versus $\omega^{-0.5}$ in the low frequency range.

of the BMM-32 electrodes was carried out. The spatially resolved capabilities of the system used allowed us to probe different particles in different electrodes, ensuring the reproducibility of the obtained results. A Raman spectrum of the uncycled electrode and two spectra recorded in cycled electrodes are shown in Fig. 10a. The latter can be considered representative of those Raman data recorded in the mentioned electrodes after cycling. Peaks appearing in the (150–1000) cm^{-1} spectral range correspond to vibration modes involving different oxides, while those observed in the (1000–2000) cm^{-1} range mainly correspond to vibrations involving carbon atoms from carbon black or carbonates formed upon cycling. This is the case of peaks centered at 1341 cm^{-1} and 1602 cm^{-1}, respectively corresponding to the well-known D and G bands of carbon black [38], and those centered at 1080 cm^{-1} and 1430 cm^{-1}, which can be tentatively attributed to symmetric and asymmetric stretching vibrations of $(CO_3)^{2-}$ anions in Li_2CO_3 [39]. The appearance of this compound is usually explained by carbonation of Li_2O in air [40]. Structural changes induced by extended cycling are more noticeable in the (700–1000) cm^{-1} range, corresponding to stretching vibrations of $[MoO_4]$ tetrahedra. The Raman spectrum of the uncycled electrode shows sharp and well-defined peaks, mostly corresponding to stretching vibrations of $[MoO_4]$ tetrahedra [20], evidencing the high crystallinity of the $Cu_3Mo_2O_9$ material. Deconvolution of this spectrum to a sum of Voigt profiles is shown in Fig. S4. Changes in the Mo-O sublattice can be clearly observed in Raman spectra of the cycled anode (charged state), revealing a loss of crystallinity of the electrode material after cycling, as evidenced by peak broadening that sometimes precludes observation of resolved bands. In addition, new peaks, not observed in spectra recorded in the uncycled electrode, are found in Raman spectra of the cycled material. These peaks rarely appear as resolved bands and can be more often observed as shoulders of bands with higher relative intensity or found by deconvolution (Fig. S4 and Table S1). One of such bands is centered at 742 cm^{-1} (marked with asterisks in Fig. 10a) and is often reported as the Raman fingerprint of MoO_2 [41], while another band at 290 cm^{-1} (marked with ex letters in Fig. 10a) can be assigned to CuO [42]. This is coherent with the proposed electrochemical mechanism in which an initial conversion reaction is followed by a diffusive process.

In addition, an *in-situ* impedance study of the pre- and post-cycled anode was carried out. Fig. 10b shows the Nyquist plots of a BMM-32 composite electrode before and after cycling (a total of 130 cycles at different current rates, following the sequence shown in Fig. 8b). These plots are composed of a depressed semicircle in the medium-high frequency range and a straight sloping line in the low frequency range. The data could be fitted considering the equivalent circuit shown in the inset of Fig. 10b. The high frequency resistance (R1 in the scheme) is related to the contribution from the electrolyte and electrode, the medium frequency resistance (R2 in the equivalent circuit) corresponds to the

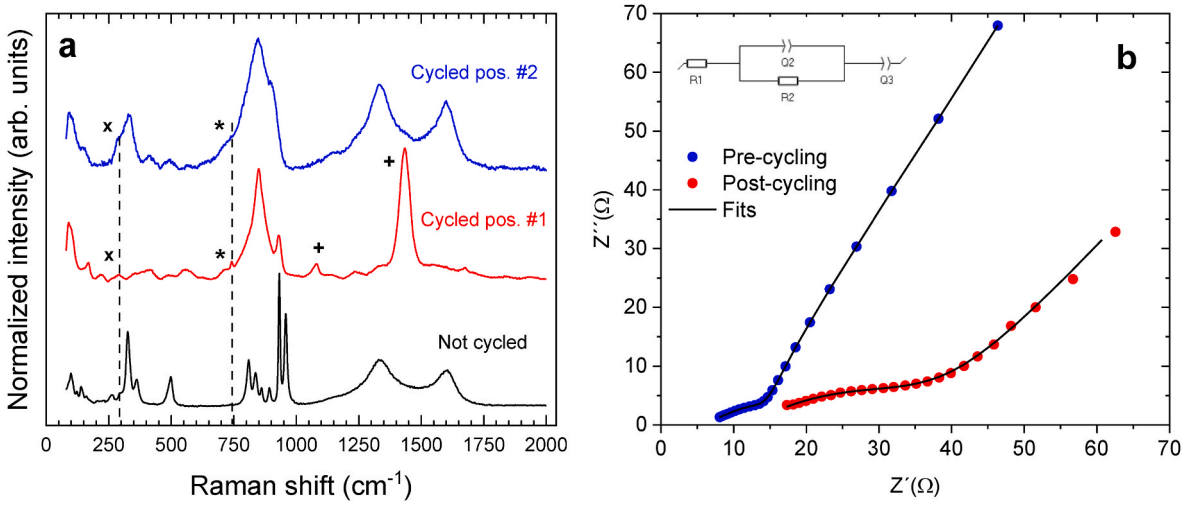

Fig. 10. a) Raman spectra recorded in a BMM-32 electrode before cycling and after 130 cycles. Signals attributed to MoO_2 (*), CuO (x) and Li_2CO_3 (+) have been marked in spectra recorded after cycling. b) Impedance Nyquist plots of the same electrode before and after cycling. The inset shows the equivalent circuit employed for fitting the experimental data.

charge transfer resistance at the electrode/electrolyte interface, and the sloped line (Warburg component) can be assigned to the solid diffusion process of lithium ions in the active material [43]. The charge-transfer resistance values obtained for the pre- and post-cycled electrode are 5.7 Ω and 28.4 Ω, respectively. This increase evidence a degradation of the ionic transport process through components and across interfaces and can be associated with the kinetic hindering caused by the enriching in insulating constituents. In summary, the cycling process causes a long-term decrease in crystallinity and an increase in the charge-transfer resistance. However, this degradation proceeds rather slowly, allowing the anode to maintain a good electrochemical performance for over 2000 cycles.

4. Conclusions

1. $Cu_3Mo_2O_9$ has been synthesized through different routes, namely coprecipitation, the solvothermal method and the solid-state method, using in this latter case either ball-milled pure metal powders or ball-milled oxide powders as precursors. The effects of each synthesis route on the morphology, structure and compositional homogeneity of the different samples were assessed, as well as their influence on the electrochemical performance as anodes for LIBs.
2. Irrespective of the synthesis conditions, long-range and short-range structural characterization - respectively carried out by XRD and micro-Raman spectroscopy - reveal the formation of single-phase, highly crystalline orthorhombic $Cu_3Mo_2O_9$, while SEM-EDS and TEM-EDS measurements indicate a homogeneous spatial distribution of the constituent elements. However, SEM and HRTEM measurements show that the growth method strongly influences particle size and morphology of the samples, ranging from flower-like or porous structures (ST-32 and Copre-32) to more compact granular textures (BMO-32 and BMM-32).
3. Regarding the electrochemical behavior, cyclic voltammetry and galvanostatic charge-discharge measurements demonstrate that $Cu_3Mo_2O_9$-based anodes show a good specific capacity and excellent cycling stability. However, clear differences in long-term performance were observed. Notably, samples obtained by mechanical milling of Cu and Mo powders followed by oxygen annealing showed a capacity of 200 mA h g^{-1} for more than 2000 cycles at a high current density of 1 A g^{-1} with coulombic efficiencies above 97 %. Such an outstanding long-term cycling performance is attributed to the high structural stability and compositional homogeneity achieved at macroscopic and local scales through the mechanical milling process. In comparison, the Copre-32 sample exhibited excellent initial capacity values but suffered from faster capacity fading, especially at higher current densities. The BMO-32 sample, although structurally similar to BMM-32, showed lower capacities and poorer retention, suggesting a lower degree of homogeneity or conductivity. Finally, the ST-32 sample presented the most porous and heterogeneous morphology, which likely facilitated electrolyte access but compromised mechanical stability over cycling.
4. Post-cycling Raman spectroscopy studies of the BMM-32 sample revealed a loss of crystallinity in the active material after prolonged cycling and allowed the identification of some phases present throughout the cycling process, thereby confirming the proposed conversion mechanism. Besides, EIS measurements indicated an increased charge transfer resistance. Despite these expected degradation effects, the electrochemical stability of the mentioned samples remained remarkably high over 2300 cycles, establishing the feasibility of $Cu_3Mo_2O_9$ as an anode material for long-life, high-rate LIB, especially when synthesized through mechanical milling of metals followed by a fine-tuned thermal oxidation treatment. This approach enables the synthesis of Cu-Mo mixed oxides with high structural stability and unprecedented cyclability for LIBs.

CRediT authorship contribution statement

J. Calbet: Writing – original draft, Methodology, Investigation, Data curation. **C. Díaz-Guerra:** Writing – review & editing, Resources, Investigation, Funding acquisition, Formal analysis, Conceptualization. **M.L. López:** Investigation, Formal analysis. **P. Almodóvar:** Methodology, Data curation. **I. Álvarez-Serrano:** Writing – review & editing, Resources, Investigation, Formal analysis, Conceptualization.

Funding

This work has been supported by UCM through project PR3/23–30813.

Declaration of competing interest

The authors declare that they have no known competing financial interests or personal relationships that could have appeared to influence the work reported in this paper.

Acknowledgments

The authors thank the UCM XRD research assistance center and the CNME ELECMI - National Center for Electron Microscopy (Spain) for scientific support.

Appendix A. Supplementary data

Supplementary data to this article can be found online at https://doi.org/10.1016/j.ceramint.2025.05.371.

References

[1] Energy Institute, Energy institute statistical review of world energy: world electricity production by source. https://www.energyinst.org/statistical-review, 2025. (Accessed 3 March 2025).
[2] M.H. Hossain, M.A. Chowdhury, N. Hossain, M.A. Islam, M.H. Mobarak, Advances of lithium-ion batteries anode materials—A review, J. Adv. Chem. 16 (2023) 100569, https://doi.org/10.1016/j.ceja.2023.100569.
[3] P.U. Nzereogu, A.D. Omah, F.I. Ezema, E.I. Iwuoha, A.C. Nwanya, Anode materials for lithium-ion batteries: a review, Appl. Surf. Sci. 9 (2022) 100233, https://doi.org/10.1016/j.apsadv.2022.100233.
[4] J. Lu, Z. Chen, F. Pan, Y. Cui, K. Amine, High-performance anode materials for rechargeable lithium-ion batteries, Electrochem. Energy Rev. 1 (2018) 35–53, https://doi.org/10.1007/s41918-018-0001-4.
[5] Y. Lu, L. Yu, X.W.D. Lou, Nanostructured conversion-type anode materials for advanced lithium-ion batteries, Chem 4 (2018) 972, https://doi.org/10.1016/j.chempr.2018.01.003.
[6] C.V. Ramana, A. Mauger, C.M. Julien, Growth, characterization and performance of bulk and nanoengineered molybdenum oxides for electrochemical energy storage and conversion, Prog. Cryst. Growth Char. Mater. 67 (2021) 100533, https://doi.org/10.1016/j.pcrysgrow.2021.100533.
[7] X. Ge, Y. Zhu, Z. Cao, J. Jia, Q. Zhao, S. Chang, S. Liu, X. Yang, K. Feng, High-specific-capacity molybdate anode materials for lithium-ion batteries with good low-temperature performance, J. Alloys Compd. 903 (2022) 163914, https://doi.org/10.1016/j.jallcom.2022.163914.
[8] P. Gong, M. Hu, Y. Zheng, S. Tao, H. Li, S. Zeng, L. Wang, Study for the construction of $CoMoO_4$ rod-like microstructures as anode material for high rate lithium-ion batteries, Mater. Chem. Phys. 333 (2025) 130207, https://doi.org/10.1016/j.matchemphys.2024.130207.
[9] L. Zhang, S. Zheng, L. Wang, H. Tang, H. Xue, G. Wang, H. Pang, Fabrication of metal molybdate micro/nanomaterials for electrochemical energy storage, Small 13 (2017) 1700917, https://doi.org/10.1002/smll.201700917.
[10] A. Rahmani, H. Farsi, Nanostructured copper molybdates as promising bifunctional electrocatalysts for overall water splitting and CO_2 reduction, RSC Adv. 10 (2020) 39037–39048, https://doi.org/10.1039/D0RA07783F.
[11] P. Almodóvar, M.L. López, J. Ramírez-Castellanos, S. Nappini, E. Magnano, J. M. González-Calbet, C.S. Díaz-Guerra, Synthesis, characterization and electrochemical assessment of hexagonal molybdenum trioxide (h-MoO_3) microcomposites with graphite, graphene and graphene oxide for lithium-ion batteries, Electrochim. Acta 365 (2021) 137355, https://doi.org/10.1016/j.electacta.2020.137355.
[12] L. Zhang, W. He, Y. Liu, M. Ling, P. Zheng, S. Guo, 3D hierarchical flower of copper molybdate $Cu_3Mo_2O_9$: synthesis, nanostructure and lithium storage properties, J. Alloys Compd. 723 (2017) 512–519, https://doi.org/10.1016/j.jallcom.2017.06.175.

[13] H. Liu, L. Liu, C. Ding, A quick microwave-assisted rheological phase reaction route for preparing $Cu_3Mo_2O_9$ with excellent lithium storage and supercapacitor performance, J. Alloys Compd. 867 (2021) 159061, https://doi.org/10.1016/j.jallcom.2021.159061.
[14] J. Xia, W. Liu, Y. Teng, L. Zhao, Q.S. Wang, M.M. Ruan, Construction of $Cu_3Mo_2O_9$ nanoplates with excellent lithium storage properties based on a pH-dependent dimensional change, Dalton Trans. 44 (2015) 13450–13454, https://doi.org/10.1039/C5DT01645B.
[15] B. Swain, D.H. Lee, J.S. Kim, C.G. Lee, D.W. Kim, K.S. Park, Synthesis of flower-like $Cu_3[MoO_4]_2O$ from $Cu_3(MoO_4)_2(OH)_2$ and its application for lithium-ion batteries: structure–electrochemical property relationships, Chemelectrochem 4 (2017) 2608–2617, https://doi.org/10.1002/celc.201700499.
[16] L. Xiaolong, G.P. Nunna, P.R. Guddeti, N.H. Alotaibi, R. Pitcheri, T.J. Ko, Binder-free $CaMoO_4$ nanostructured anode electrodes for Li-ion battery applications, Ceram. Int. 50 (2024) 31491–31503, https://doi.org/10.1016/j.ceramint.2024.05.456.
[17] Z. Wang, S. Madhavi, X.W. Lou, Ultralong α-MoO_3 nanobelts: synthesis and effect of binder choice on their lithium storage properties, J. Phys. Chem. C 116 (2012) 12508–12513, https://doi.org/10.1021/jp304216z.
[18] P. Almodóvar, D. Giraldo, C. Díaz-Guerra, J. Ramírez-Castellanos, J.M. González Calbet, J. Chacón, M.L. López, h-MoO_3/$AlCl_3$-urea/Al: high performance and low-cost rechargeable Al-ion battery, J. Power Sources 516 (2021) 230656, https://doi.org/10.1016/j.jpowsour.2021.230656.
[19] P. Almodóvar, I. Álvarez-Serrano, I. Llorente, M.L. López, J. Chacón, C. Díaz-Guerra, Nickel-doped h-MoO_3 cathodes: a high-performance material for aluminum-ion batteries, Batter. Energy (2025), https://doi.org/10.1002/bte2.20240076.
[20] B. Saravanakumar, G. Ravi, R. Yuvakkumar, V. Ganesh, R.K. Guduru, Synthesis of polyoxometalates, copper molybdate ($Cu_3Mo_2O_9$) nanopowders, for energy storage applications, Mater. Sci. Semicond. Process. 93 (2019) 164–172, https://doi.org/10.1016/j.mssp.2019.01.002.
[21] Y. Zhang, G. Zhao, Y. Jiang, W. Hong, Y. Zhang, M. Deng, X. Ji, Monocrystal $Cu_3Mo_2O_9$ confined in polyaniline protective layer: an effective strategy for promoting lithium storage stability, Chemelectrochem 6 (2019) 1688–1695, https://doi.org/10.1002/celc.201801753.
[22] B. Sotillo, J. Calbet, I. Álvarez-Serrano, I. García-Díaz, P. Fernández, F.A. López, Exploring titanium niobium oxides recovered from columbotantalite mineral as lithium-ion batteries electrodes, Ceram. Int. 50 (2024) 32783–32792, https://doi.org/10.1016/j.ceramint.2024.06.088.
[23] Y. Gogotsi, R.M. Penner, Energy storage in nanomaterials–capacitive, pseudocapacitive, or battery-like? ACS Nano 12 (2018) 2081–2083, https://doi.org/10.1021/acsnano.8b01914.
[24] J. Wang, J. Polleux, J. Lim, B. Dunn, Pseudocapacitive contributions to electrochemical energy storage in TiO_2 (anatase) nanoparticles, J. Phys. Chem. C 111 (2007) 14925–14931, https://doi.org/10.1021/jp074464w.
[25] P. Sirisinudomkit, P. Iamprasertkun, A. Krittayavathananon, T. Pettong, P. Dittanet, M. Sawangphruk, Hybrid energy storage of $Ni(OH)_2$-coated N-doped graphene aerogel//N-doped graphene aerogel for the replacement of NiCd and NiMH batteries, Sci. Rep. 7 (2017) 1124, https://doi.org/10.1038/s41598-017-01191-8.
[26] T. Li, S. Gao, K. Li, G. Liu, X. Sheng, D. Shang, S. Wu, Tailoring the phase evolution of molybdenum-based nanocrystals in carbon nanofibers for enhanced performance of lithium-ion batteries, J. Alloys Compd. 934 (2023) 168042, https://doi.org/10.1016/j.jallcom.2022.168042.
[27] W. Li, J.A. Quirk, M. Li, W. Xia, L.M. Morgan, W. Yin, X. Sun, Precise tailoring of lithium-ion transport for ultralong-cycling dendrite-free all-solid-state lithium metal batteries, Adv. Mater. 36 (2024) 2302647, https://doi.org/10.1002/adma.202302647.
[28] M. Yao, H. Zhang, K. Dong, B. Li, C. Xing, M. Dang, S. Zhang, Ultralong cycling and wide temperature range of lithium metal batteries enabled by solid polymer electrolytes interpenetrated with a poly (liquid crystal) network, J. Mater. Chem. A 9 (2021) 6232–6241, https://doi.org/10.1039/D0TA10932K.
[29] X. Cheng, F. Ran, Y. Huang, R. Zheng, H. Yu, J. Shu, Y.B. He, Insight into the synergistic effect of N, S co-doping for carbon coating layer on niobium oxide anodes with ultra-long life, Adv. Funct. Mater. 31 (2021) 2100311, https://doi.org/10.1002/adfm.202100311.
[30] G. Wang, Z. Wen, L. Du, Y.E. Yang, S. Li, J. Sun, S. Ji, Hierarchical Ti–Nb oxide microspheres with synergic multiphase structure as ultra-long-life anode materials for lithium-ion batteries, J. Power Sources 367 (2017) 106–115, https://doi.org/10.1016/j.jpowsour.2017.09.061.
[31] J.-L. Do, T. Friščić, Mechanochemistry: a force of synthesis, ACS Cent. Sci. 3 (2017) 13–19, https://doi.org/10.1021/acscentsci.6b00277.
[32] I. Jonane, A. Cintins, A. Kalinko, R. Chernikov, A. Kuzmin, Low temperature X-ray absorption spectroscopy study of $CuMoO_4$ and CuMo0.90W0.10O4 using reverse Monte-Carlo method, Radiat. Phys. Chem. Oxf. Engl. 175 (2020) 108411, https://doi.org/10.1016/j.radphyschem.2019.108411.
[33] E. Botcharova, J. Freudenberger, L. Schultz, Mechanical alloying of copper with niobium and molybdenum, J. Mater. Sci. 39 (2004) 5287–5290, https://doi.org/10.1023/B:JMSC.0000039230.73188.5d.
[34] B. Niu, Q. Liu, L. Liu, J. Ni, R. Ren, Q. Li, J. He, Influence of powder ball milling pretreatment on microstructure and properties of Mo-W-Cu refractory functional alloys sintered in a normal-pressure hydrogen atmosphere, Powder Technol. 438 (2024) 119625, https://doi.org/10.1016/j.powtec.2024.119625.
[35] W. Zhao, B. Yan, P. Li, D. Chen, H. Guo, Z. Liu, M. Chu, Interface behavior and oxidation consolidation mechanism of titanium-bearing iron sand particles with ball-milling pretreatment, Powder Technol. 396 (2022) 366–377, https://doi.org/10.1016/j.powtec.2021.11.008.
[36] D.Q. Yi, C.P. Wu, S. Goto, C.H. Xu, J. Li, B. Wang, F. Zheng, Influence of ball-milling on the oxidation behavior of Ag–Zn alloy powders, Mater. Corros. 61 (2010) 590–598, https://doi.org/10.1002/maco.200905334.
[37] Q. Xia, H. Zhao, Z. Du, Z. Zeng, C. Gao, Z. Zhang, K. Świerczek, Facile synthesis of MoO_3/carbon nanobelts as high-performance anode material for lithium-ion batteries, Electrochim. Acta 180 (2015) 947–956, https://doi.org/10.1016/j.electacta.2015.09.042.
[38] M. Pawlyta, J.-N. Rouzaud, S. Duber, Raman microspectroscopy characterization of carbon blacks: spectral analysis and structural information, Carbon 84 (2015) 479–490, https://doi.org/10.1016/j.carbon.2014.12.030.
[39] P. Pasierb, S. Komornicki, M. Rokita, M. Rękas, Structural properties of Li_2CO_3–$BaCO_3$ system derived from IR and raman spectroscopy, J. Mol. Struct. 596 (2001) 151–156, https://doi.org/10.1016/S0022-2860(01)00703-7.
[40] D. Ensling, A. Thissen, W. Jaegermann, On the formation of lithium oxides and carbonates on Li metal electrodes in comparison to $LiCoO_2$ surface phases investigated by photoelectron spectroscopy, Appl. Surf. Sci. 255 (2008) 2517–2523, https://doi.org/10.1016/j.apsusc.2008.07.196.
[41] M. Dieterle, G. Mestl, Raman spectroscopy of molybdenum oxides. Part II. Resonance raman spectroscopic characterization of the molybdenum oxides Mo_4O_{11} and MoO_2, Phys. Chem. Chem. Phys. 4 (2002) 822–826, https://doi.org/10.1039/B107046K.
[42] L. Debbichi, M.C. Marco de Lucas, J.F. Pierson, P. Krüger, Vibrational properties of CuO and Cu_4O_3 from first-principles calculations, and raman and infrared spectroscopy, J. Phys. Chem. C 116 (2012) 10232–10237, https://doi.org/10.1021/jp303096m.
[43] L.A. Middlemiss, A.J. Rennie, R. Sayers, A.R. West, Characterization of batteries by electrochemical impedance spectroscopy, Energy Rep. 6 (2020) 232–241, https://doi.org/10.1016/j.egyr.2020.03.029.